Journal of Nuclear Materials 389 (2009) 203–212

Contents lists available at ScienceDirect

Journal of Nuclear Materials

journal homepage: www.elsevier.com/locate/jnucmat

A description of stress driven bubble growth of helium implanted tungsten

Shahram Sharafat [a,*], Akiyuki Takahashi [b], Koji Nagasawa [b], Nasr Ghoniem [a]

[a] University of California Los Angeles, CA 90095-1597, USA
[b] Tokyo University of Science, Chiba, Japan

A B S T R A C T

Low energy (<100 keV) helium implantation of tungsten has been shown to result in the formation of unusual surface morphologies over a large temperature range (700–2100 °C). Simulation of these macroscopic phenomena requires a multiscale approach to modeling helium transport in both space and time. We present here a multiscale helium transport model by coupling spatially-resolved kinetic rate theory (KRT) with kinetic Monte Carlo (KMC) simulation to model helium bubble nucleation and growth. The KRT-based HEROS Code establishes defect concentrations as well as stable helium bubble nuclei as a function of implantation parameters and position from the implanted surface and the KMC-based Mc-HEROS Code models the growth of helium bubbles due to migration and coalescence. Temperature- and stress-gradients can act as driving forces, resulting in biased bubble migration. The Mc-HEROS Code was modified to simulate the impact of stress gradients on bubble migration and coalescence. In this work, we report on bubble growth and gas release of helium implanted tungsten W/O stress gradients. First, surface pore densities and size distributions are compared with available experimental results for stress-free helium implantation conditions. Next, the impact of stress gradients on helium bubble evolution is simulated. The influence of stress fields on bubble and surface pore evolution are compared with stress-free simulations. It is shown that near surface stress gradients accelerate helium bubbles towards the free surface, but do not increasing average bubble diameters significantly.

1. Introduction

The divertor plates in magnetic fusion energy (MFE) devices, such as ITER have to withstand high heat and low energy ion fluxes, and the first wall of inertial fusion energy (IFE) reactor chambers have to mitigate the effects of high temperature pulses and high energy ion implantation. During the normal operation, in the ITER divertor zone steady state plasma parameters are expected to be ~5–20 MW m^{-2} heat, ~10^{24} H^+ m^{-2} s^{-1} (1–10 eV) protons, and ~10^{22}–10^{24} He^{2+} m^{-2} s^{-1} (<500 eV) helium ions [1–3]. In contrast, a 10 m radius IFE chamber, such as the high average power laser (HAPL) reactor [4] is expected to be exposed to helium and deuterium ions ranging in energy from 1 keV to 10 MeV, with a low energy helium flux of about ~10^{15} m^{-2} in the range of 100–200 keV and a high energy helium flux of ~10^{16} m^{-2} between 200 keV and 10 MeV (per shot from a 365 MJ target). For both applications, tungsten is chosen as a primary candidate armor material, because of high temperature capabilities, relatively high thermal conductivities, good sputtering erosion resistance, and near zero tritium retention [5,6]. However, there is compelling experimental evidence that low and high energy helium implantation of tungsten can result in drastic changes in the surface morphology over a wide temperature range [7–12]. Therefore, helium implantation in tungsten has become the subject of significant R&D activities for ITER divertor development [7–12], IFE chamber wall protection [13,15], and non-refractory neutron irradiated alloys [16].

Helium transport is further complicated in an IFE chamber, because the first wall experiences large, pulsed heat loads at frequencies of several hertz. The heating is caused by a succession of X-rays, neutrons, and ions arriving at the first wall within a few microseconds. The volumetric deposition of these particles is confined to within a few microns from the surface [15]. For a chamber radius of 7 m with no protective gas, temperatures at the surface of the implanted region of a tungsten first wall (FW) armor can reach about 2500 °C, resulting in large stress gradients and plastic deformation or cracking [17].

The evolution of helium bubbles or blister formation in implanted materials is a multiscale process in both space and time. Present day computational performance limitations do not allow simulation of microstructural evolution over engineering-relevant time scales (hours and beyond) starting with first principle calculations. Instead, an atomistic-to-continuum modeling method based on decoupled sequential simulation of energetics/kinetics, defect formation/clustering, and microstructural feature formation is employed. Pertinent information from the finer scale simulation is transferred to the next coarser but less computationally demanding scale. Of the aforementioned simulation methods, the

* Corresponding author. Tel.: +1 310 794 5990; fax: +1 310 206 4830.
E-mail address: shahrams@ucla.edu (S. Sharafat).

0022-3115/$ - see front matter © 2009 Elsevier B.V. All rights reserved.
doi:10.1016/j.jnucmat.2009.02.027

cluster dynamics scale requires the smallest computational resources, and can be used to investigate reactor lifetime scale phenomena and processes [18].

Traditionally, helium cluster dynamic modeling during irradiation has been based on chemical rate theory also referred to as Master Equation [18–21]. Conventional kinetic rate-theory models assume strictly homogeneous field parameters and as such cannot directly resolve space-dependent phenomena on helium transport. A spatially -resolved kinetic rate theory was developed, called the HEROS Code [22,23], which is capable of simulating complex transient and space-dependent helium transport in finite geometries, including the simultaneous production of defects and space- and time-dependent temperature and temperature gradients. Space-dependent nucleation and growth of helium bubbles during implantation can be modeled including the impact of biased helium bubble migration.

In this work, we report on our modeling results, based on using spatially-resolved kinetic rate theory (HEROS Code) to estimate the helium bubble nucleation rate, which is then transferred to the kinetic Monte Carlo (KMC) simulation code to model bubble evolution due to migration and coalescence of equilibrium He-bubbles during implantation. The KMC code is called Mc-HEROS, which stands for Monte Carlo simulation-based helium bubble evolution and resolution. In developing the Mc-HEROS Code, we closely followed the methodology, first reported by Evans et al. [24], who simulating surface bubble growth during annealing of helium implanted Cu. Based on our earlier work [25] we first demonstrate that the Mc-HEROS simulations agree very well with experimental results observed in low energy helium tungsten implantation experiments. Next, we describe the newly developed formulism added to the Mc-HEROS Code to simulate the effects of stress gradient on biased migration of helium bubbles. The impact of prolonged, near surface stress gradients on transport, migration, and coalescence of helium bubbles during annealing is then compared with stress-free simulations.

2. Experimental observations

Fig. 1 summarizes recent (2000 – present) helium implantation experiments in support of ITER tungsten divertor [26] and HAPL first wall tungsten armor development. Helium implantation energies range from a few eV to several MeVs, and target temperatures vary between 300 and 2600 K. Implantation fluence is not reflected on this summary chart.

At moderate surface temperatures <1000 K low energy (<100 keV) helium implantation can form blisters and cause exfoliation of μm-thick layers of tungsten, above a threshold fluence of $\sim 2 \times 10^{21}$ m^{-2} and $\sim 10^{22}$ m^{-2}, respectively [9,13,27,28]. At higher temperatures (>1000 K), implantation of low energy (10 eV < E_{He} < 60 keV) helium ions to fluences above $\sim 10^{20}$ m^{-2} has been shown to produce extensive oversized surface pinholes [8–10], form micron-size 'coral' type surface structures between ~1400 and 2600 K [9,13,14], or cover the surface with low density nano-thick tungsten-wool structures when exposed to 60 eV helium between 1100 and 1300 K [12].

Nishijima et al. [29] showed that at ~1873 K (1600 °C) implantation of tungsten with helium ions having energies as low as 10 eV results in the formation of large micron-sized surface pores. Although at 10 eV the implantation depth of helium in tungsten is of the order of only a few lattice constants (~10 Å), micron-sized bubbles were observed several micrometers below the surface. Furthermore, the implantation energy of 10 eV was well below the displacement energy of tungsten (60–80 eV [32]). Formation of oversized surface pinholes was also observed, whose density and size distributions were found to depend on surface temperatures as well as helium energies. Helium bubbles were also formed with incident helium energies only slightly above the surface barrier potential of ~6 eV [29].

Implantation with 19 keV Helium at temperatures of ~1273 K (800 °C) resulted in the formation of large blisters with a diameter of 0.5–1.0 μm at fluences of 1.7×10^{22} He/m^2 [9]. However, at high temperatures 2873 K (2600 °C) the same implantation conditions resulted in the formation of a 'coral structured' tungsten surface, with 'coral horns' protruding several micrometers above the surface.

In support of the HAPL project [4], the IEC facility at UW-Madison has investigated low energy helium implantation in tungsten [13,14] (IEC: inertial electrostatic confinement [30]). Formation of oversized surface bubbles along with drastic surface morphology changes were observed [14] when tungsten was exposed to a helium plasma with energies less than 60 keV and temperatures between 1000 and 1450 K. Fig. 2 shows micrographs of tungsten surfaces implanted with lower energy (30 keV) helium between 1000 and 1450 K at the UW-Madison IEC facility [31]. At a nominal fluence of $\sim 3 \times 10^{22}$ He/m^2, the average surface pore diameter were 30, 120 and 170 nm at 1003 (730 °C), 1263 (990 °C), and 1433 K (1160 °C), respectively. With increasing temperatures, surface pore diameter increases, while pore densities drop which implies significant helium bubble coalescence.

Neutron irradiation of metals can result in helium generation by transmutation reactions, involving the host atoms and neutrons. In a recent study, helium was injected into low activation oxide

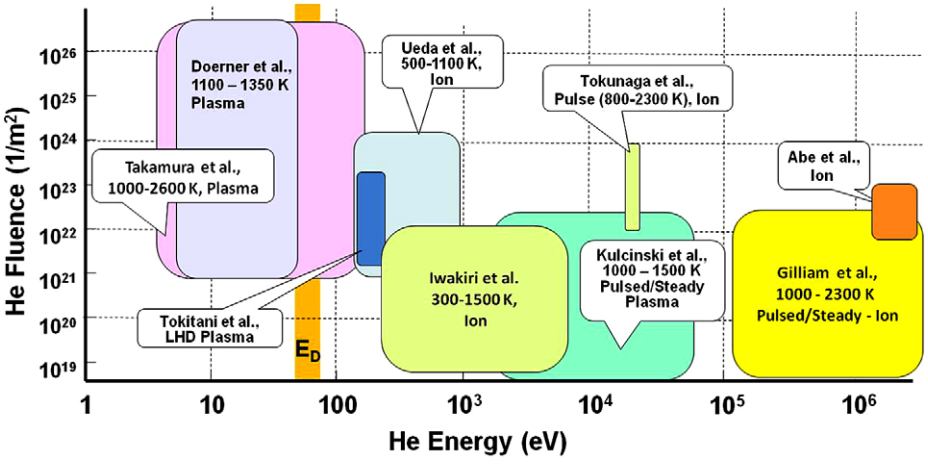

Fig. 1. Summary of Japanese and US helium implantation experiments in support of ITER divertor development [26]; added: Kulcinski and Gilliam representing HAPL-IFE Chamber wall development activities (E_D indicates the range of crystal-orientation dependent displacement energy for tungsten. 60–80 eV [32]).

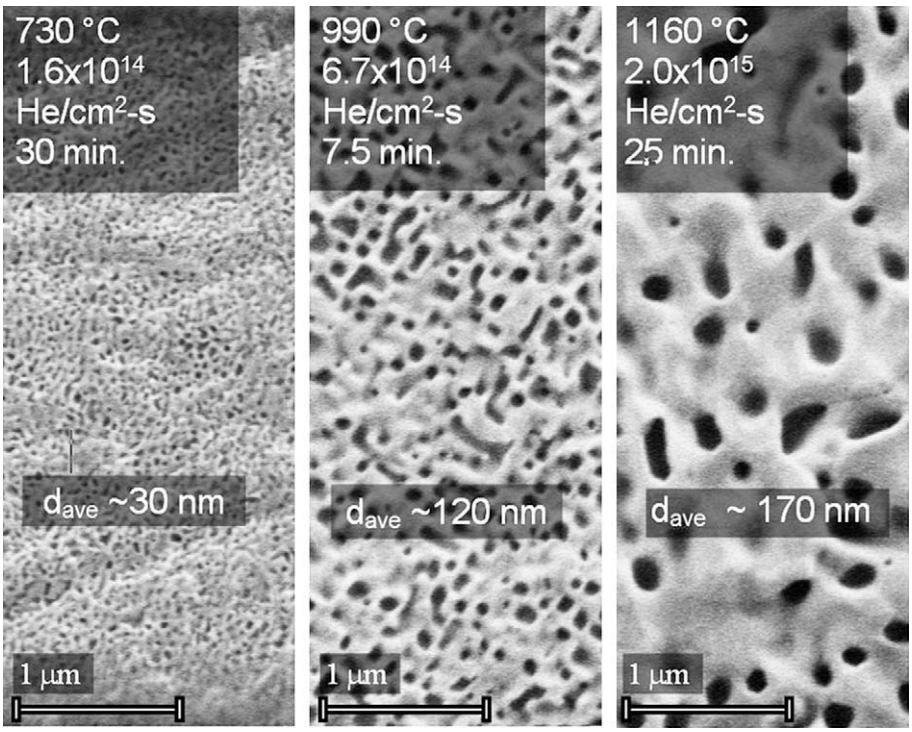

Fig. 2. Micrographs of tungsten surfaces implanted with low energy (30 keV) He at the UW-Madison IEC facility [31].

dispersed strengthened (ODS) iron-based alloys using the $^{59}Ni(n_{th}, a)$ reactions to study the impact of nano-size precipitates on helium bubble density and size distribution [16]. It was shown that the presence of large densities of fine particles, significantly suppressed helium bubble growth by 'trapping' small bubbles (<1 nm radius) at the nano-size particles.

3. Bubble evolution model

At elevated temperatures ($T > 0.3\ T_m$; T_m is melt temperature) helium bubble evolution in metals during irradiation can be broadly divided into two distinct stages: nucleation and growth [33]. The IEC helium implantation experiments [13,14] are performed at 730, 990, and 1160 °C, which are below and above 0.3 T_m of tungsten (for tungsten 0.3 T_m = 848 °C). The nucleation phase of helium bubbles is modeled using kinetic rate theory (HEROS Code) and the growth phase is modeled using kinetic Monte Carlo simulation (Mc-HEROS Code) via migration and coalescence. First, a short description of the HEROS and the Mc-HEROS transport models is given.

3.1. HEROS Code transport model

Reaction-rate-theory has been widely used to analyze dynamic radiation effects in materials at elevated temperatures [18–21]. Ghoniem et al. [20] derived a set of hierarchical Master Equations (MEs), which successfully modeled the loss of helium to grain boundaries during irradiation. Later Sharafat et al. [21] augmented the MEs to include the effects of cascade induced interstitial- (CIIC) and vacancy clusters (CIVC). In the presence of helium these clusters were shown to have a significant effect on the bubble nucleation rate.

However, these kinetic rate-theory models assume strictly homogeneous field parameters and as such cannot directly resolve space-dependent phenomena on helium transport. Recently, a new approach to simulate space-dependent helium transport during irradiation in finite geometries was developed, by augmenting the MEs with Drift and Diffusion terms [22,23]. The model and the numerical code, called HEROS Code is thus capable of simulating spatially dependent processes, such as occur during implantation near surfaces.

The HEROS Code uses a set of 13 Master Equations to model the evolution of the following 13 species: (1) unoccupied single vacancies; (2) single self-interstitial atoms; (3) interstitial helium atoms; (4) substitutional helium atoms; (5) di-interstitial helium atom clusters; (6) di-helium single vacancy clusters; (7) bubble nuclei (containing three helium atoms w/o a single vacancy); (8) large bubbles containing m helium atoms. Furthermore, five equations are used to analyze the (9) average matrix bubble size; (10) average number of helium atoms in a matrix bubble; (11) amount of helium absorbed in grain boundaries; (12) average precipitate bubble radius; and (13) amount of helium in precipitate bubbles. In addition, the HEROS Master Equations analyze the sink-loss term associated with precipitate densities and grain boundaries. It is assumed, that on average each precipitate has one helium bubble attached to it. For a detail derivation of the spatially homogeneous rate equations the reader is referred to [22]. The HEROS Code also includes extensive bubble kinetics models, based on surface- and volume diffusion mechanisms as well as Brownian Motion and biased migration.

By discretizing space, this set of Master Equations can be solved to simulate both, spatial- and time-dependent processes. The HEROS Codes discretizes space into predefined spatial bins and then solves the ME's within each bin, while keeping track of all mobile species fluxes across bin boundaries. Although within each spatial bin the ME's are solved using homogeneous field parameters, the net flux of migrating species across the bins imparts a space-dependent simulation of the microstructure evolution as a function of space and time. Provided the spatial bin sizes are chosen fine enough, such that the details and the extent of external driving forces are captured, the solution will simulate space-dependent processes. By discretizing space, the flux of mobile species crossing

bin boundaries are modeled with respective diffusion and drift components. Thus, the HEROS Code is capable of simulating the transport of mobile species through space.

3.2. Mc-HEROS Code transport model

Details of the Mc-HEROS Code computational algorithm and structure will be reported elsewhere [34], here we will outline some of the fundamental bubble kinetics aspects of the Mc-HEROS Code. The kinetics of bubble migration and coalescence in the absence of driving forces, are based on Brownian Motion. Both surface- and volume diffusion of bubbles are included, however at IEC relevant temperatures surface diffusion is the predominant diffusion mechanism [35]:

$$D_B = \frac{3\Omega^{4/3}}{2\pi r^4} D_S, \tag{1}$$

where D_B is the bubble diffusion coefficient, Ω is the atomic volume, r is the bubble radius and D_S is the surface diffusion coefficient, defined as $D_s = D_o \exp(-E_s/kT)$, where D_0 is the pre-exponential and E_S is the surface activation energy. Surface activation energies and associated pre-exponential factors for Tungsten were reported by Ehrlich et al. [36]. Depending on the crystollographic plane, surface activation energies range from 19.0 to 42.0 kcal/mol (0.92–1.82 eV). At 1000 K the surface diffusivity of W is $\sim 5.8 \times 10^{-8}$ cm^2/s.

The coalescence process of two bubbles assumes that once they touch, the volumes of the two bubbles will merge and their pressure will be in equilibrium with the surface tension instantaneously ($p = 2\gamma/R$) [24]. The equilibrium condition requires that the newly formed bubble instantaneously grows in size to accommodate the high internal pressure. For small bubbles, inside the matrix helium gas pressures indicating solid state conditions have been measured for matrix bubbles in nickel and aluminum [37]. Furthermore, at elevated pressures, plastic deformation of the material surrounding the bubble can occur, which would result in slowing down or even self-pinning of the bubble.

However, for near surface bubbles, these high pressure conditions generally do not exists because of the abundance of large number of vacancies produced due to the vicinity of a free surface. Chernokiv et al. [38], measured the mean radius of helium bubbles in Ni as a function of annealing temperature near the surface and in the bulk. Near surface (<1 μm from the surface) bubbles had radii of the order of 70 nm, while the radii of matrix bubbles (>3 μm deep) were only 2 nm. IEC helium implantation energies are between 30 and 60 keV, which results in implantation depths of less than 0.2 μm in tungsten. Furthermore, SRIM calculations indicate that on average about 38–56 vacancies are produced per implanted helium between 30 and 60 keV, respectively. Thus, because of the abundance of near surface- and ion-generated vacancies in IEC implantation conditions, helium bubbles readily grow to equilibrium sizes with low helium pressures (vacancies are captures by bubbles, allowing them to grow rapidly to equilibrium sizes).

4. Modeling surface pores of He-implanted tungsten

The HEROS Code (rate-theory based) was used to estimate helium bubble nucleation based on the steady state UW-Madison IEC implantation conditions of 30 keV helium up to fluences of 3×10^{22} He/m^2 in tungsten. The implanted tungsten sample is about $1 \times 1 \times 1$ cm^3 and is suspended inside the plasma chamber [14]. Because of the high thermal conductivity of tungsten (~120 W/m K at 1000 K), temperatures can be assumed to be uniform throughout in the implantation region. The implantation profile was estimated using SRIM-2003 SRIM Monte Carlo computer program with a maximum at ~0.1 μm. In tungsten, about nine vacancies are produced per 30 keV Helum ion. The ample supply of vacancies combined with the large helium implantation rates promotes bubble nucleation and bubble radii are driven based on $p = 2\gamma/R$, where γ is the surface tension of tungsten and R is the bubble radius.

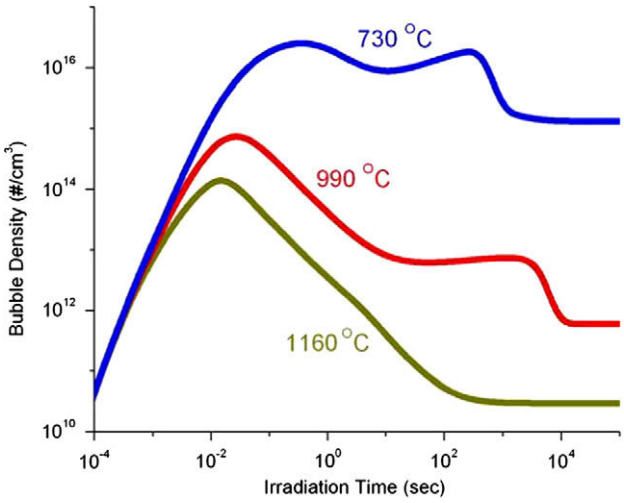

Fig. 3. Helium bubble density evolution in tungsten as a function of implantation time for IEC conditions (E_{He} = 30 keV, fluence ~3×10^{21} He/m^2).

During the IEC implantation experiments, helium is continuously added to the material. Multi-species helium-vacancy clusters form and continue to trap helium atoms, which leads to formation of stable He-bubble nuclei. IEC implantation conditions at 730, 990, and 1160 °C are listed in Table 1 and Fig. 3 shows estimated bubble densities as calculated by the HEROS Code. Depending on the surface temperature bubble density peaks occur between ~10^{-2} s and 1 s, following the onset of implantation. It is interesting to note that stable bubble nuclei densities saturate in less than 1 s, depending on temperature. As shown in Fig. 3, nucleation of new bubbles is eventually suppressed because growing bubbles provide strong sinks for the newly implanted helium ions. Thus, nucleation of new bubbles ceases once maximum densities of stable nuclei have been reached. The helium bubble growth phase, can now be modeled using the KMC simulation (Mc-HEROS Code) using the rate-theory based nucleation results.

4.1. Conditions at onset of bubble growth

The initial condition of the KMC simulation for bubble growth assumes that the stable bubble nuclei are distributed with a Gaussian over the implantation range, with a peak at ~0.1 μm for 30 keV helium in W (IEC conditions). Furthermore, it is assumed that at the start of the simulation all bubbles have the same average bubble radius, which was calculated by the HEROS Code to be between 0.5 and 1.5 nm, depending on temperature. Table 1 lists the parameters used in the KMC simulation.

4.2. Simulation results in stress-free surfaces

The Mc-HEROS simulation time sequence of helium bubble growth for IEC helium implantation conditions (730 °C, 30 keV [13,31]) is shown in Fig. 4. The color scheme is chosen such that matrix bubbles are light and bubbles that touch or penetrate the surface are colored dark. It is observed that within ~ 1 min (68 s) the first surface pores appear and after ~2000 s (at the end of the implantation cycle) almost all of the bubbles have pierced the surface.

Table 1
Parameters used for the KMC simulation of helium bubble growth for IEC low energy implantation experiments with tungsten [31].

Tungsten surface temperature (°C)	Helium implantation (10^{18}/m^2 s)	Implantation time (s)	Bubble density (cm^{-3})	Bubble radius (nm)	Simulation volume (mm^3)
730	1.6	1800	10^{17}	0.5	$0.2 \times 1.0 \times 1$
990	6.7	450	10^{15}	1.0	$0.2 \times 2.5 \times 1$
1160	20.0	150	10^{14}	1.5	$0.2 \times 5.0 \times 1$

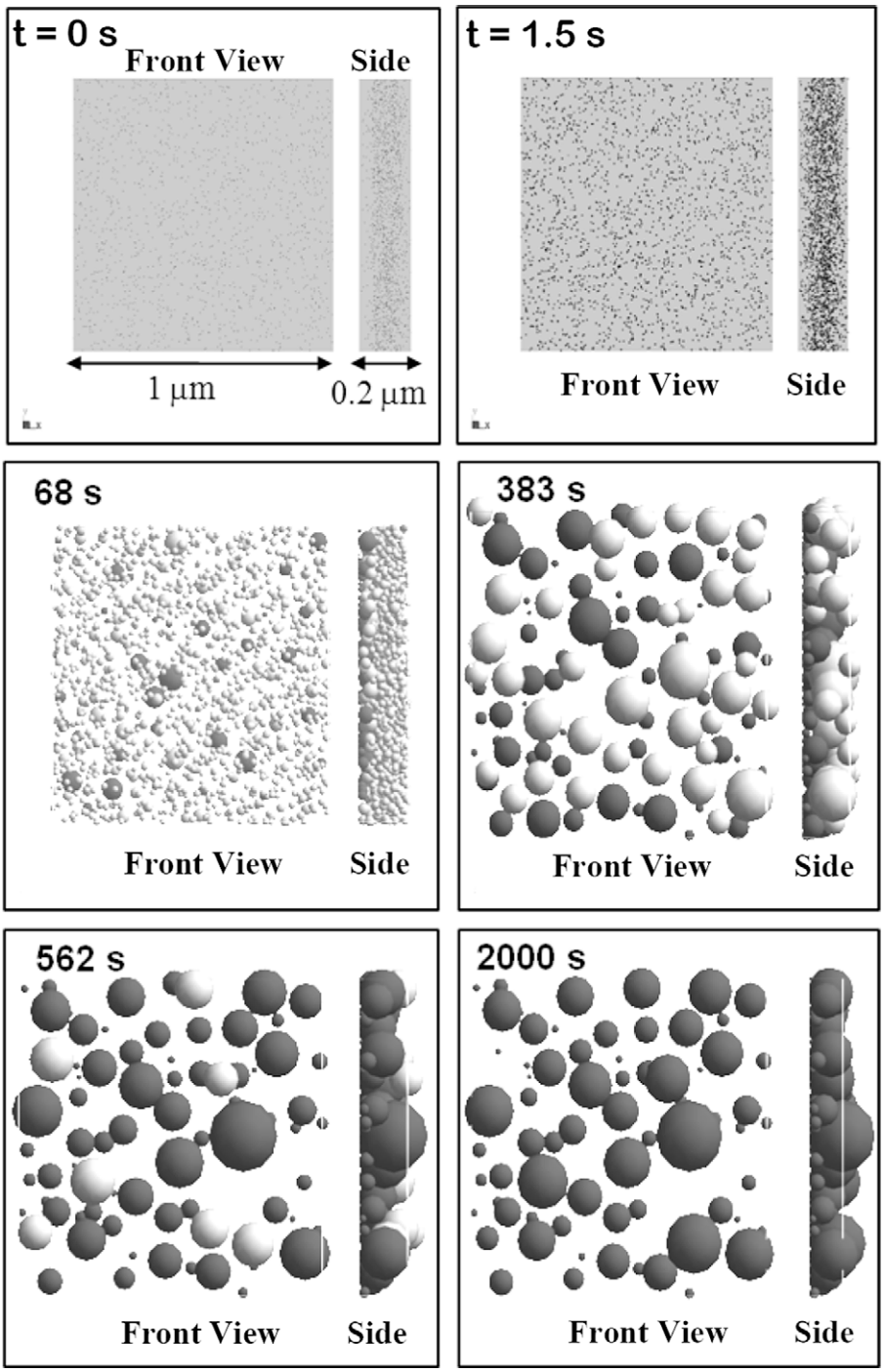

Fig. 4. Snap shots of the time sequence of the KMC simulation results of the IEC helium implantation condition at $T = 730$ °C, 1.6×10^{18} He/m^2 s, $E_{He} = 30$ keV; (light colored spheres represent matrix or bulk bubbles; dark spheres represent surface pores or bubbles that have penetrated the top surface).

As a of result rapid bubble growth rates, the bubble densities inside the simulation volume ($1 \times 1 \times 0.2$ μm^3) decreased sharply. To maintain a large enough statistical sampling, a cloning process was adopted as suggested by Evans et al. [24]. It consists of simply doubling the simulation volume as soon as bubble concentrations fall below a threshold value of about 5000 bubbles.

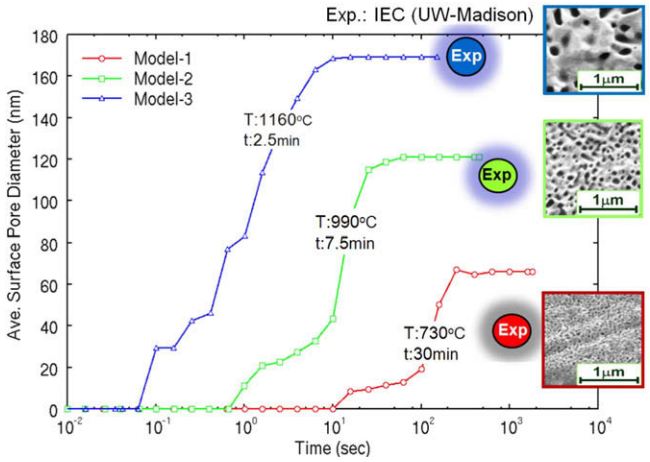

Fig. 5. KMC simulation of surface bubble average diameter as a function of implantation time in low energy helium implanted tungsten at various temperatures and implantation rates (IEC implantation. E_{He} = 30 keV, helium fluence ~3 × 10^{21} He/m^2 [14,31]).

Fig. 5 shows the evolution of average diameter of surface pores for all three test temperatures (760, 990, and 1160 °C). A comparison with IEC experimental results indicates that the Mc-HEROS calculated average surface pore diameters agree well at 990 and 1160 °C. At 730 °C simulated pore diameters are about 50% larger than experimental results. The reason is the fundamental assumption of separating helium bubble nucleation and growth phases into two distinct phases. Below $T \sim .3\ T_m$ (730 °C is below 0.3 T_m for tungsten) this assumption is no longer valid. Thus, during implantation experiments at 730 °C nucleation of new helium bubbles continues during the growth phase, resulting in higher number densities of surface pores with associated smaller average diameters. Consequently, our assumption that nucleation of new bubble is absent during the bubble growth stage results in larger average helium bubble radius compared with experimental measurements.

5. Influence of stress gradients on bubble evolution

The response of bubble evolution to a stress field was modeled using the KMC simulation. Implantation of ions, particularly in IFE armored chamber first walls is associated with large temperature and stress gradients, resulting from the high surface heat flux and ion implantation. A unified materials response code (UMARCO) was recently developed to model the combined effects of spectra of ions, X-rays, and neutrons on temperature, stress, and strain fields near the surface of an IFE chamber wall [39]. The impact of H, D, T, He, and C ion implantation and X-rays on heating rate is estimated and consequent strain- and stress transients were calculated. Fig. 6 shows surface strain and stress transients and snapshots of depth profiles in tungsten resulting from a single shot in a 10 m radius IFE chamber (365 MJ DT target). The surface of a tungsten armor

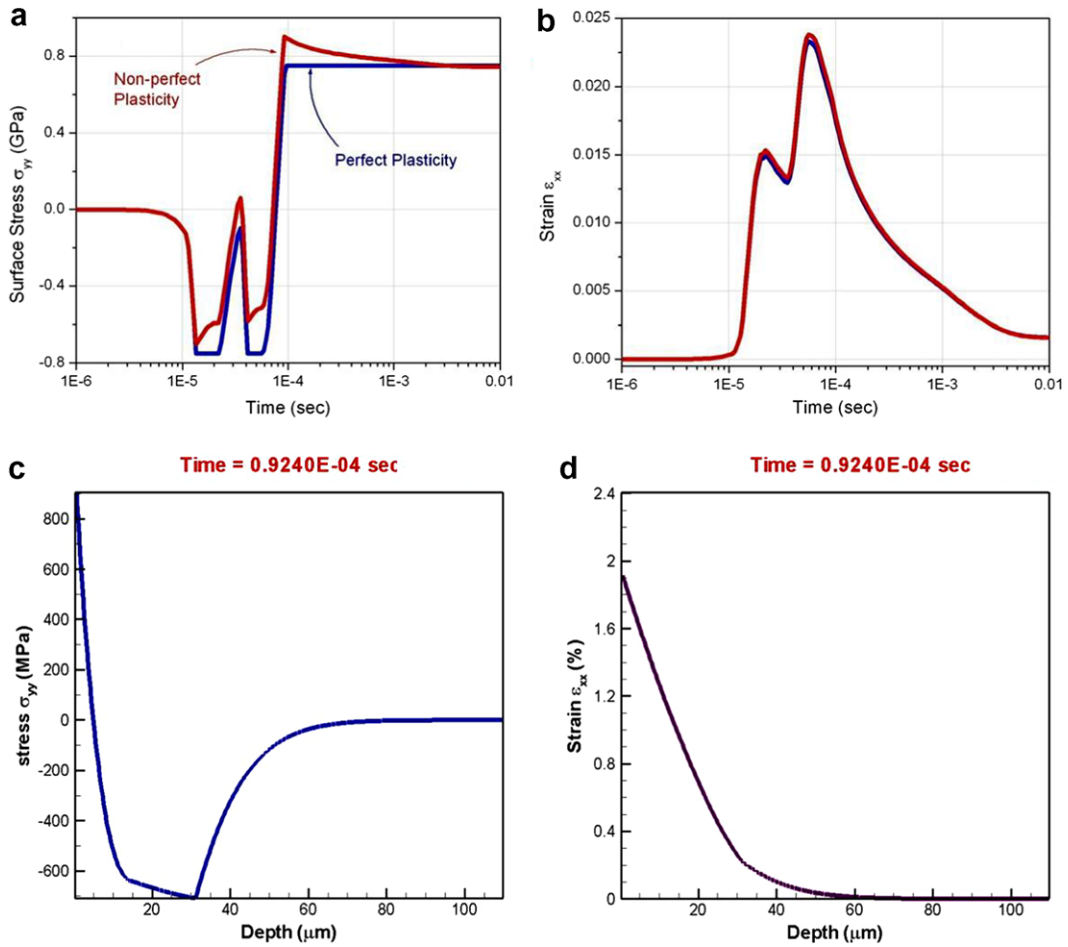

Fig. 6. Surface stress (a) and strain (b) transients on the surface along with snapshots of stress (c) and strain (d) depth profiles in tungsten resulting from a single shot in a 10 m radius IFE chamber following a 365 MJ DT target burn.

reaches maximum stress of ~0.8 GPa and strain of about ~2.4%, stresses. Stress gradients as high as 1.4×10^6 MPa/m (140 MPa/μm) develop within the first 10 microns from the free surface at about 9×10^{-5} s after the burn. Although these rapid transients are very rapid ($< 10^{-3}$ s), the residual stress and strain fields as high as 800 MPa and 0.2% remain near the surface.

5.1. KMC modeling of stress gradient on bubble migration

In modeling the influence of stress gradients on bubble migration, we follow the formulism of Leiden et al. [40]. The influence of stress on pore migration in solids was modeled by estimating the change in elastic strain energy of a spherical pores with internal pressures being balanced by surface tension as it moves from a lower stress to higher stressed region in the solid. The associated total energy decrease implies a thermodynamic force tending to drive the bubble in the direction of higher stress, whether it is tensile or compressive. The magnitude of this force determines the speed of bubble migration.

The migration velocity (V_p) of a spherical pore in a stress-free solid is given by:

$$V_p = B_p F_p, \tag{2}$$

and

$$B_p = \frac{D_p}{kT} = \frac{3a_0\Omega}{2\pi kTr^4} D_S, \tag{3}$$

where B_P is pore mobility based on the pore surface diffusion mechanism, F_P is the driving force, D_p is pore diffusion coefficient, k is Boltzmann's constant, T is temperature in K, a_0 is the lattice constant, Ω is

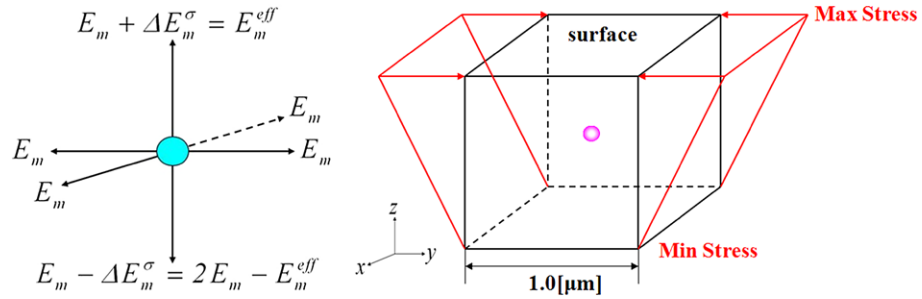

Fig. 7. Right. schematic of the KMC simulation volume with a stress gradient and a bubble at its center; left: schematic of pore migration energies in a uni-axial stress gradient in the z-direction (E_m is the migration energy of pore, ΔE_m^σ is the change in migration energy due to stress).

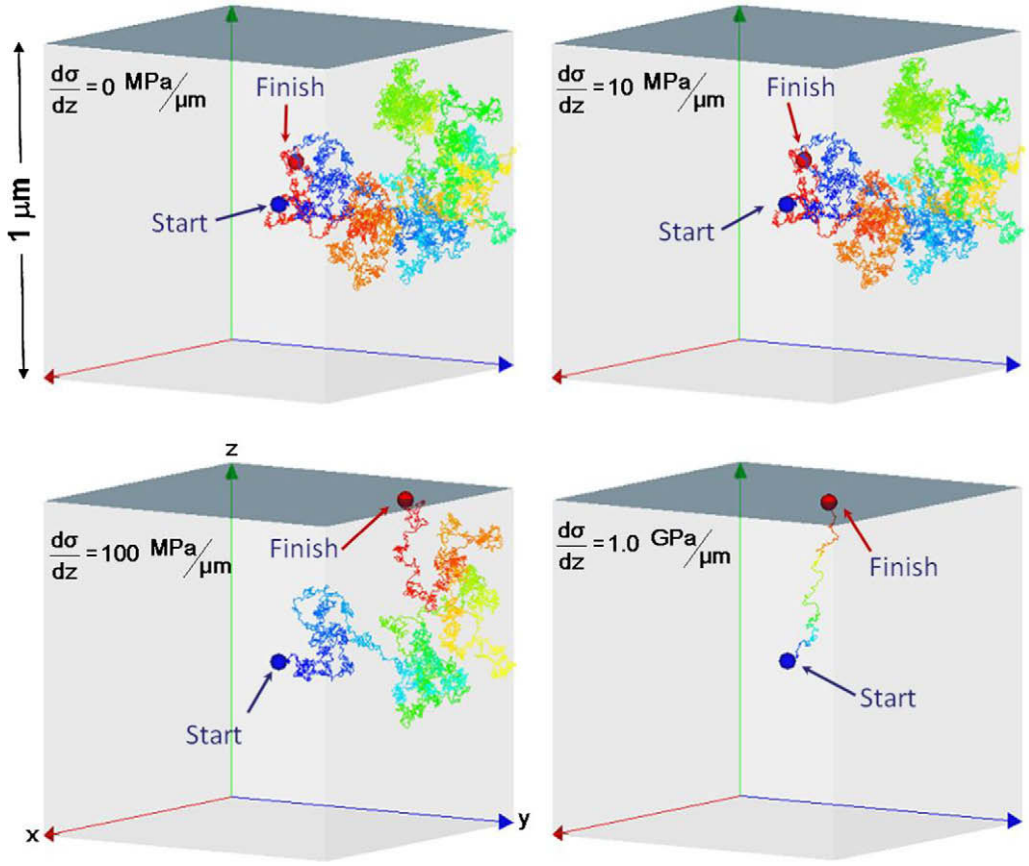

Fig. 8. KMC simulation of influence of a uni-axial stress gradient on the migration of a single (5 nm diameter) helium bubble in tungsten at 1300 K (initial position. filled blue dot; final position. filled red dot). (For interpretation of the references to colour in this figure legend, the reader is referred to the web version of this article.)

the molecular volume of the diffusing species, r the pore radius and D_s the surface diffusion coefficient for a pore (see Eq. (1)).

To calculate the migration velocity of a pore (V_p) along a stress gradient, the influence of the stress gradient on the mobility (B_p) and the force (F_p) have to be determined. Assuming that a uni-axial stress gradient acts along the z-direction, the force (F_p) acting on a pore is based on the change in elastic energy (ΔE_{tot}) along the z-direction is given by [40]:

$$F_p = -\frac{\partial \Delta E_{tot}}{\partial z} = v_b \times 3\partial \times \sigma/E \times \partial\sigma/\partial z, \tag{4}$$

where v_b is bubble volume, ∂ is a constant based on an algebraic expression involving the Poisson's ratio ($\sim$3.02 for $\nu = 0.3$), σ is the stress and z the direction perpendicular to the stress gradient.

The diffusion of a pore can be approximated by an 'effective' migration energy due to the presence of a stress gradient as follows: the three-dimensional mean-square distance (x_p^2) traveled by a pore in time t is:

$$x_p^2 = 6D_p t = 6kTB_p t, \tag{5}$$

where the value in any specified direction is given by $2kTB_p t$. Using the pore velocity (V_p) and pore mean-square distance (x_p^2) the effective diffusion coefficient and hence the effective pore migration energy is defined by:

$$D_p^{\text{eff}} = V_p\sqrt{x_p^2} = D_0 \exp\left(-E_m^{\text{eff}}/kT\right). \tag{6}$$

Thus, taking a time step (t) an effective migration energy E_m^{eff} can be estimated from D_p^{eff}. The difference in migration energy due to a stress gradient (ΔE_m^{σ}) can be expressed as:

$$\Delta E_m^{\sigma} = E_m^{\text{eff}} - E_m. \tag{7}$$

Fig. 7 depicts schematically the directional migration energies of a bubble inside a solid with a uni-axial stress-gradient along the z-direction. Details of the computational aspects of the KMC simulation of the Mc-HEROS Code will be published elsewhere [34].

5.2. Single bubble migration in a stress gradient

First, the effect of a stress gradient on the migration of a single 5 nm radius helium bubble in tungsten at 1300 K was studied. The test volume was a cube with 1 μm sides. Fig. 8 depicts the schematic of the KMC simulation volume with an imposed stress gradient and a bubble at its center. Minimum stress was kept at 0.0 MPa and maximum stress was varied from 0 to 1 GPa. The simulation was run for a duration of up to 2.5×10^6 s. Stress gradients of up to 10 MPa/μm seem to have no discernible influence on bubble migration, and the bubble comes to rest within 0.2 μm from its original location. For stress gradients above 100 MPa/μm a 1 nm radius bubble migrates up the stress gradient and reaches the surface within $\sim 3.7 \times 10^7$ s and 1.67×10^6 s for 100 and 1000 MPa/μm. The effect of bubble radius migrating through a stress gradient was also investigated. Bubbles with 1, 3, and 5 nm radius were exposed to different stress gradients and times to reach the free surface increased with increasing bubble size.

5.3. Combined migration and coalescence of bubbles in a stress gradient

The influence of a stress gradient on migration and coalescence of a collection of bubbles was simulated by assuming a Gaussian

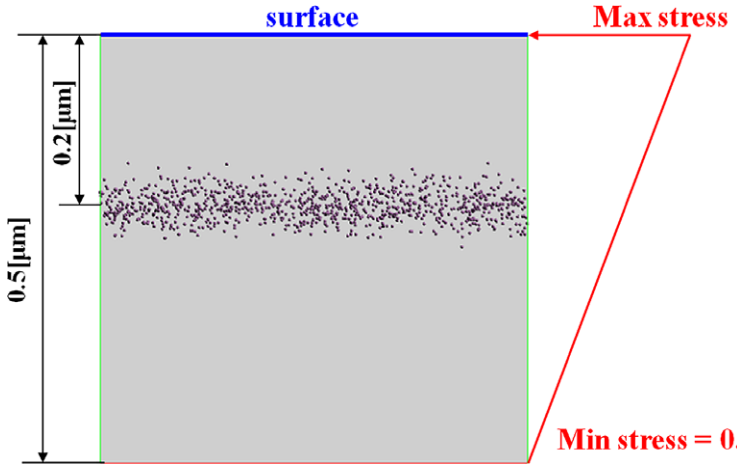

Fig. 9. Initial condition for the KMC simulation of the effect of stress gradient on the collective behavior of helium bubbles (number of initial bubbles 1000; average bubble radius 1.84 nm).

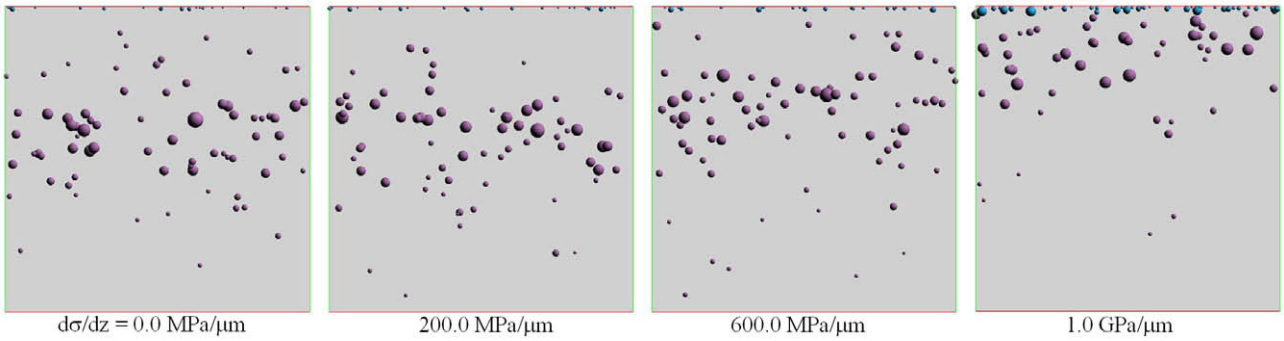

Fig. 10. KMC simulation results showing final bubble distribution after 3 × 107 s for various stress gradients at 1300 K in tungsten (initial bubble profile is shown in Fig. 9).

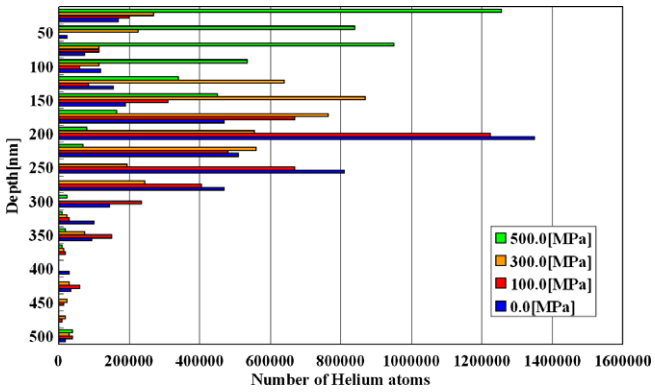

Fig. 11. Influence of stress gradient on final helium atom distribution as a function of depth after 3×10^7 s in tungsten at 1300 K (initial conditions are shown in Fig. 9).

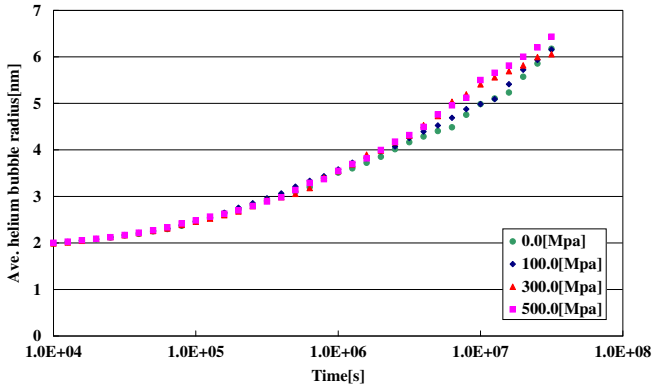

Fig. 12. Average helium bubble radius in 0, 200, 600, and 1000 MPa/mm stress gradient in tungsten at 1300 K.

distribution at 0.05–0.2 μm below the surface with a peak at 0.2 μm. The number of initial bubbles was 1000 with an average bubble radius of 1.84 nm and the maximum stress was 0, 100, 300, and 500 MPa over 0.5 μm (see Fig. 9). Fig. 10 shows the final stages of helium bubble distribution below the surface for stress gradients ranging from 0.0 to 1.0 GPa/μm. As expected, the stress gradient drives the collective bubble population towards the free surface or up the stress gradient. Fig. 11 shows the final helium atom distribution as a function of depth from the high stressed surface after 3×10^7 s. For higher stress gradients, more helium bubbles appear near or on the surface.

Fig. 12 shows the average helium radius as a function of annealing time for the different stress gradients. The average helium bubble size triples from ~2 to ~6 nm. Note, that compared with stress-free KMC simulations (Figs. 4 and 5) the average bubble radius increase is insignificant. Bubble velocity decreases with increasing bubble radius proportional to $1/r^4$ based on a surface diffusion mechanism (Eq. (3)). However, in a stress gradient field the driving force increases with bubble size proportional to r^3 (Eq. (4)). Thus, the migration velocity of a bubble in a stress gradient is proportional to $1/r$. In other words, the stress gradient reduces the relative velocity between dissimilarly sized bubbles, bubble growth rates due to coalescence between small and large bubbles is also reduced.

6. Conclusions

Implantation of tungsten with low energy He ions results in the unusual formation of large numbers of oversized surface pores, which eventually result in drastic changes of the tungsten surface morphology. Low energy (30 keV) Helium implantation experiments between 800 and 980 °C with helium implantation doses of $\sim 6 \times 10^{21}$ m^{-2} resulted in the formation of surface pores with average diameters of about 130 nm and a density of $\sim 7 \times 10^{12}$ m^{-2}.

To model the formation of these oversized surface pores, a helium transport model was developed, which combines kinetic rate theory (KRT) based helium bubble nucleation with kinetic Monte Carlo (KMC) simulation of bubble migration and coalescence. We developed a KMC-based code (Mc-HEROS Code) to model equilibrium helium bubble kinetics using surface diffusion and Brownian Motion migration and coalescence. Saturated bubble nuclei densities were estimated using the KRT-based HEROS Code and used as initial bubble distributions in the Mc-HEROS KMC code. The abundance of vacancies due to near-surface proximity of the bubbles (<200 nm) and due to ion-implantation generated vacancies supplies abundant vacancies for coalescing bubbles to attain equilibrium size and pressure instantaneously.

Experimental results of helium–plasma implanted tungsten were simulated using the hybrid KRT and KMC approach. Surface pore size and densities agreed very well with experimental observations. The experimentally observed surface morphology changes are thus explained by rapid helium bubble migration and coalescence rates near the implanted surface.

The effect of stress gradients on bubble migration and coalescence was simulated using the Mc-HEROS Code (KMC). It was shown that for single small bubbles (<5 nm radius) stress gradients of larger than 100 MPa/μm are necessary to influence bubble migration significantly at 1300 K in tungsten. We also noted an interesting interplay between bubble size and stress gradient: as the bubble size increases, bubble velocity (v_s) due to surface diffusion mechanism decreases (v_s $1/r^4$), while the velocity (v_{sg}) due to the stress gradient increases (v_{sg} r^3). Thus, the net velocity of a bubble in a stress gradient is proportional to $1/r$. Therefore, the relative velocities between dissimilarly sized bubbles is reduced in a stress gradient field and smaller bubbles no longer travel much faster compared with larger bubble in a stress-free matrix.

The influence of stress gradients on the kinetics of a collection of bubbles was also investigated. The KMC simulation volume contained a Gaussian distribution of about 1000 bubbles with an average bubble radius of 1.84 nm with a peak density at about 0.2 μm below the surface in tungsten at 1300 K. As expected, the average bubble radii increased from about 2 nm to about 6 nm regardless of stress gradients level. As expected, the KMC simulation shows that with an increase in stress gradient the collection of bubbles moves more rapidly to the free surface.

Acknowledgements

This work was sponsored by the Naval Research Laboratory NNSA/DP (HAPL Project) and the US Department of Energy Office of Fusion Science and Energy (Fusion Materials Development) and the Tokyo University of Science, Chiba Japan.

References

[1] B. de Groot, R.S. Al, R. Engeln, W.J. Goedheer, O.G. Kruijt, H.J.V.D. Meiden, P.R. Prins, D.C. Schram, P.H.M. Smeets, V.P. Veremiyenko, W.A.J. Vijvers, J. Westerhout, A.W. Kleyn, N.J. Lopes Cardozo, G.J. van Rooij, Fus. Eng. Des. 82 (15–24) (2007) 1861.
[2] C.H. Wu, C. Alessandrini, J.P. Bonal, J.W. Davis, A.A. Haasz, W. Jacob, A. Kallenbach, J. Keinonen, P. Kornejew, R. Moormann, V. Philipps, J. Roth, F. Scaffidi-Argentina, H. Würz, Fus. Eng. Des. 56&57 (2001) 179.
[3] R. Behrisch, G. Federici, A. Kukushkin, D. Reiter, J. Nucl. Mater. 313–316 (2003) 388.
[4] John D. Sethian, A. Rene Raffray, Jeffery Latkowski, James P. Blanchard, Lance Snead, Timothy J. Renk, Shahram Sharafat, J. Nucl. Mater. 347 (3) (2005) 161.

[5] J.W. Davis, V.R. Barabash, A. Makhankov, L. Plochl, K.T. Slattery, J. Nucl. Mater. 258–263 (1998) 308.
[6] R.E. Nygren, D.L. Youchison, R.D. Watson, S. O_Dell, Fus. Eng. Des. 49&50 (2000) 303.
[7] M. Tokitani, M. Miyamoto, D. Koga, K. Tokunaga, T. Fujiwara, N. Yoshida, S. Masuzaki, N. Ashikawa, T. Morisaki, M. Shoji, A. Komori, J. Nucl. Mater. 337–339 (2005) 937.
[8] N. Yoshida, H. Iwakiri, K. Tokunaga, T. Baba, J. Nucl. Mater. 337–339 (2005) 946.
[9] K. Tokunaga, S. Tamura, N. Yoshida, K. Ezato, M. Taniguchi, K. Sato, S. Suzuki, M. Akiba, J. Nucl. Mater. 329–333 (2004) 757.
[10] D. Nishijima, T. Sugimoto, H. Iwakiri, M.Y. Ye, N. Ohno, N. Yoshida, S. Takamura, J. Nucl. Mater. 337–339 (2005) 927.
[11] W.M. Shu, G.-N. Luo, T. Yamanishi, J. Nucl. Mater. 367–370 (2) (2007) 1463.
[12] M.J. Baldwin, R.P. Doerner, Nucl. Fus. 48 (2008) 035001.
[13] B.B. Cipiti, G.L. Kulcinski, J. Nucl. Mater. 347 (3) (2005) 298.
[14] R.F. Radel, G.L. Kulcinski, J. Nucl. Mater. 367–370 (1) (2007) 434.
[15] Shahram Sharafat, Nasr M. Ghoniem, Michael Anderson, Brian Williams, Jake Blanchard, Lance Snead, J. Nucl. Mater. 347 (3) (2005) 217.
[16] T. Yamamoto, G.R. Odette, P. Miao, D.T. Hoelzer, J. Bentley, N. Hashimoto, H. Tanigawa, R.J. Kurtz, J. Nucl. Mater. 367–370 (1) (2007) 399.
[17] James P. Blanchard, Carl J. Martin, J. Nucl. Mater. 347 (3) (2005) 192.
[18] S. Sharafat, N.M. Ghoniem, Radiat. Eff. Def. Solids 113 (4) (1990) 331, doi:10.1080/10420159008213077.
[19] M. Kiritani, J. Phys. Soc. Jpn. 36 (1973) 95.
[20] N.M. Ghoniem, J.N. Alhajji, J. Nucl. Mater. 136 (1985) 192.
[21] S. Sharafat, N.M. Ghoniem, J. Nucl. Mater. 283 (789) (2000).
[22] S. Sharafat, Q. Hu, N.M. Ghoniem, HEROS: A Spatial- and Temporal Helium Bubble Evolution and Resolution Code (to be submitted).
[23] Qiyang Hu, Shahram Sharafat, Nasr M. Ghoniem, Fus. Sci. Technol. 52 (3) (2007) 574.
[24] J.H. Evans, R. Escobar Galindo, A. van Veen, Nucl. Instrum. and Meth. Phys. Res. B 217 (2004) 276.
[25] A. Takahashi, S. Sharafat, J. Kulcinski, R. Radel, N. Ghoniem, in: Presented at the ANS 17th Topical Meeting on the Technology of Fusion Energy – TOFE-2006, Albuquerque, New Mexico, November 13–16, 2006.
[26] UEDA, private communications, March, 2008.
[27] E.L. Fleischer, M.G. Norton, Heterogen. Chem. Rev. 3 (1996) 171.
[28] S.K. Erents, G.M. McCracken, Radiat. Eff. Def. Solids 18 (3) (1973) 191.
[29] D. Nishijima, M.Y. Ye, N. Ohno, S. Takamura, J. Nucl. Mater. 329–333 (2004) 1029.
[30] G.H. Miley, Y. Gu, J. DeMora, M. Ohnishi, Fus. Eng. Des. 41 (1998) 461.
[31] B.B. Cipiti, R.F. Radel, G.L. Kulcinski, in: Presented at the Ninth High Average Power Laser Program Workshop, 2–3 June 2004, University of California Los Angeles, Los Angeles, CA, USA. (also in B.B. Cipiti, G.L. Kulcinski, J. Nucl. Mater. 347(3) (2005) 298).
[32] R.N. Stuart, M.W. Guinan, R.J. Borg, Radiat. Eff. Def. Solids 30 (3) (1976) 129, doi:10.1080/00337577608233054.
[33] H. Trinkaus, B.N. Singh, J. Nucl. Mater. 323 (2003) 229.
[34] A. Takahashi, k. Nagasawa, S. Sharafat (to be submitted).
[35] F.A. Nichols, J. Nucl. Mater. 30 (1969) 143.
[36] G. Ehrlich, Surf. Sci. 246 (1991) 1.
[37] W. Jager, R. Manzke, H. Trinkaus, G. Crecelius, R. Zeller, J. Fink, H.L. Bay, J. Nucl. Mater. 111&112 (1982) 674.
[38] V.N. Chernikov, H. Trinkaus, P. Jung, H. Ullmaier, J. Nucl. Mater. 170 (1990) 31.
[39] Q. Hu, M. Andersen, S. Sharafat, A. Takahashi, J. Blanchard, N. Ghoniem, in: Presented at the 17th High Average Power Laser Program Workshop, Naval Research Laboratory, Washington, DC, USA, October 30–31, 2007.
[40] S.H. Leiden, F.A. Nichols, J. Nucl. Mater. 38 (1971) 309.